JCI insight

An in vivo model of glioblastoma radiation resistance identifies long non-coding RNAs and targetable kinases

Christian T. Stackhouse, Joshua C. Anderson, Zongliang Yue, Thanh Nguyen, Nicholas J. Eustace, Catherine P. Langford, Jelai Wang, James R. Rowland IV, Chuan Xing, Fady M. Mikhail, Xiangqin Cui, Hasan Alrefai, Ryan E. Bash, Kevin J. Lee, Eddy S. Yang, Anita B. Hjelmeland, C. Ryan Miller, Jake Y. Chen, G. Yancey Gillespie, Christopher D. Willey

JCI Insight. 2022. https://doi.org/10.1172/jci.insight.148717.

Research In-Press Preview Oncology

Graphical abstract

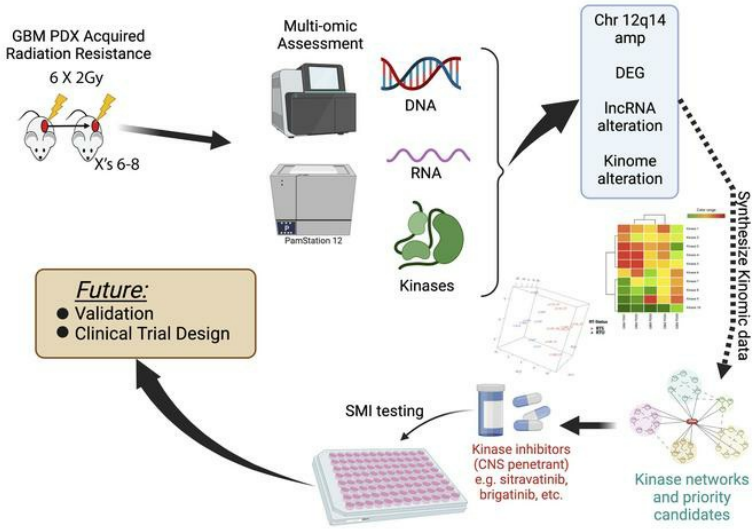

Find the latest version:

https://jci.me/148717/pdf

Title. **An in vivo model of glioblastoma radiation resistance identifies long non-coding RNAs and targetable kinases**

Authors: Christian T. Stackhouse[1,2], Joshua C. Anderson[2], Zongliang Yue[3], Thanh Nguyen[3], Nicholas J. Eustace[2], Catherine P. Langford[1], Jelai Wang[3], James R. Rowland IV[4], Chuan Xing[2], Fady M. Mikhail[5], Xiangqin Cui[6], Hasan Alrefai[2], Ryan E. Bash[7], Kevin J. Lee[2], Eddy S. Yang[2], Anita B. Hjelmeland[8], C. Ryan Miller[7], Jake Y. Chen[3], G. Yancey Gillespie[1], Christopher D. Willey[2]

Affiliations: University of Alabama at Birmingham Department of Neurosurgery, Birmingham, AL, USA[1]; University of Alabama at Birmingham Department of Radiation Oncology, Birmingham, AL, USA [2]; University of Alabama at Birmingham Informatics Institute, Birmingham, AL, USA [3]; The Ohio State University Department of Physics, Columbus, OH, USA[4]; University of Alabama at Birmingham Department of Genetics, Birmingham, AL, USA [5]; Emory University Department of Biostatistics and Bioinformatics, Atlanta, GA, USA[6]; University of Alabama at Birmingham Department of Pathology, Division of Neuropathology, Birmingham, AL, USA [7]; University of Alabama at Birmingham Department of Cell, Developmental, and Integrative Biology, Birmingham, AL, USA [8]

Corresponding Author:

Christopher D. Willey, MD, PhD Email: cwilley@uabmc.edu, Phone: (205)934-5670,

Mailing Address: Hazelrig-Salter Radiation Oncology Center RM 2232C, 619 19th Ave S, Birmingham, AL 35249

Running title (60 characters): A GBM PDX model reveals novel mechanisms of radioresistance

Keywords: Glioblastoma, radiation-resistance, DNA damage repair, long non-coding RNA, Patient-derived xenograft (PDX), kinomics

Funding: UAB Bridge Funding, U01CA223976, 3U01 CA223976-03S1, Mahaley fund

Conflict of Interest: The authors declare the following conflicts of interest: While there are no direct conflicts of interest related to the subject of this manuscript, for full disclosure, Dr. Willey declares part time consultancy for LifeNet Health, Inc., rare speaker or consultancy for Varian Medical Systems, and research funding from Varian Medical Systems, AACR-Novocure, and OMS Foundation.

Additional information:

Number of figures in main text: 6

Number of tables in main text: 0

Number of supplemental figures: 6

Number of supplemental tables: 0

Number of supplemental files: 5

ABSTRACT:

Key molecular regulators of acquired radiation resistance in recurrent glioblastoma (GBM) are largely unknown with a dearth of accurate pre-clinical models. To address this, we generated 8 GBM patient-derived xenograft (PDX) models of acquired radiation therapy-selected (RTS) resistance compared with same-patient, treatment naïve (RTU) PDX. These unique models mimic the longitudinal evolution of patient recurrent tumors following serial radiation therapy. Indeed, while whole exome sequencing confirmed retention of major genomic alterations in the RTS lines, we did detect a chromosome 12q14 amplification that is associated with clinical GBM recurrence in two RTS models. A novel bioinformatics pipeline was applied to analyze phenotypic, transcriptomic and kinomic alterations, which identified long non-coding RNAs (lncRNAs) and targetable, PDX-specific kinases. We observed differential transcriptional enrichment of DNA damage repair (DDR) pathways in our RTS models which correlated with several lncRNAs. Global kinomic profiling separated RTU and RTS models, but pairwise analyses indicated that there are multiple molecular routes to acquired radiation-resistance. RTS model-specific kinases were identified and targeted with clinically relevant small molecule inhibitors (SMIs). This unique cohort of in vivo radiation therapy-selected patient-derived models will enable future preclinical therapeutic testing to help overcome the treatment resistance seen in GBM patients.

Brief Summary: This study describes a panel of acquired radiation resistant GBM PDX and identifies potentially targetable transcriptomic (including lncRNA) and kinomic alterations.

INTRODUCTION

Glioblastoma (GBM) is the most common and devastating form of primary brain cancer. Median survival remains around 15 months despite decades of research (1). Standard adjuvant therapy for GBM includes 6-weeks of fractionated radiotherapy (RT) (typical total dose around 60 Gy) with concomitant systemic therapy using the alkylating agent temozolomide (TMZ) (75 mg/m^2 daily), followed by 6-12 months of adjuvant TMZ (150-200 mg/m^2 for 5 days every 28 days) (2). While O^6-methylguanine-DNA methyltransferase (MGMT) promoter methylation is a known predictive marker for GBM response to TMZ (3), there are no validated predictive or prognostic molecular indicators for radiotherapy response in GBM (4). GBM almost invariably recurs, and recurrent tumors frequently acquire resistance to conventional therapies. In recent years, several potential radiation resistance mechanisms have been postulated including transcriptional reprogramming (5), epigenetics (6), and cell state plasticity (7), irradiation changes to normal brain tissue (8, 9), metabolic alterations (10), and epithelial-mesenchymal transition (11) to name a few. Still, there is a dearth of accurate preclinical models, especially of recurrent, therapy-resistant tumors which are in most cases responsible for patient mortality (12).

Here we have generated 8 pairs of GBM patient-derived xenografts (PDXs) in which the radiation sensitive, unselected (RTU) tumors were irradiated for in vivo serial selection to create recurrent, radiation therapy-selected (RTS) variant PDXs. This models a common therapeutic strategy whose outcomes unfortunately lead to acquired therapy-resistance in patients (13). These patient-matched, paired PDXs allow the comparison of primary and recurrent tumors to better understand the trajectories of molecular mechanisms in tumor recurrence.

Two recent longitudinal studies in glioma have reported that selective pressures and driver mutations tend to occur early in glioma development with little change at the genomic level

following recurrence (14, 15). This may suggest that phenotypic changes such as acquired therapy resistance are not driven at the genomic level, but instead at the epigenetic, transcriptomic and post-translational levels. To this end, we have conducted whole exome sequencing (WES) as well as deep RNA sequencing (RNA-Seq) of total RNA in order to study transcripts including long non-coding RNAs (lncRNAs). LncRNAs can act as molecular sponges for microRNAs or transcription factors, scaffolds for enhancer or repressive complexes, guides for chromatin remodeling enzymes, or as signals for gene activation (16, 17). The Pan-Cancer Analysis of Whole Genomes (PCAWG) consortium has recently identified 122 lncRNAs with causal roles in cancer tumorigenesis, a number of which overlap with our results (18).

In order to identify lncRNAs and their potential targets, we have devised a novel in silico approach utilizing quasi-mapping of long, paired end reads (19) combined with nucleic acid binding prediction software using thermodynamics-based algorithms to detect RNA:RNA duplex or RNA:DNA triplex formation (20, 21) (see Methods section). We also combine traditional differential gene expression analysis (DE) with differential gene correlation analysis (DGCA) (22), machine learning (23, 24), and semantic network construction (25, 26) to further elucidate transcriptional mechanisms of therapy resistance. These approaches have revealed differential regulation of DNA damage response (DDR) pathways as well as stemness, cell cycle, and chromatin remodeling signatures. We have noted differential enrichment of canonical DDR pathways at the transcriptomic level in vivo post selection. A number of lncRNAs are associated with the differential expression of transcripts in these pathways.

We evaluated our RTS models by integrating global kinase (kinomic) activity and transcriptomic data to identify radiation-induced changes in baseline signaling and expression. Kinase signaling is highly therapeutically targetable in neoplasms (27) and radiation therapy has been

demonstrated to induce malignant phenotypes through modulation of Src and Trk family kinase signaling among others (28, 29). Our results confirmed that radiation therapy selection induced targetable kinase activity alterations. Clinically used small molecule inhibitors (SMI) sitravatinib and brigatinib (30, 31), with known brain penetrance were effective RTS GBM models. The application of our integrated informatics approach using these clinically relevant models, provides a method for selecting preclinical therapies for intractable, therapy resistant tumors.

RESULTS

Serial in vivo radiation of GBM PDX generates radiation therapy-selected (RTS) derivatives

A cohort of 20 heterotopic (subcutaneous) GBM PDX were screened for sensitivity to radiation. Tumor growth was measured externally using calipers and radiation response was defined as 'resistant' (n=8) if the median-doubling time of the initial tumor volume was significantly less than 20 days, or 'sensitive' (n=10) for doubling times greater than 20 days, or 'intermediate' (n=2) if not significantly different from 20 days (**Figure 1A**). Of these, existing Affymetrix transcriptomic microarray data were available for 13 PDX lines (n=7 sensitive, n=6 resistant). We found that 18 genes were significantly up regulated, and 8 genes were significantly down regulated in the inherent resistant group (**Supplementary Figure S1A**). Over representation analysis of these 26 genes revealed no significant enrichment at an FDR of <0.05, therefore we took the top 10 results (**Supplementary Figure S1B**). CXCR3 receptor binding was the top result driven by the significant down regulation of ligands CXCL10 and CXCL11 in inherent resistant PDX. Protein binding was the most enriched molecular function GO term followed by ion binding (**Supplementary Figure S1C**). The top enriched gene set from GSEA using the MSigDB H and C6 sets was hallmark coagulation, but the BCAT.100_UP.V1_DN set was also significantly enriched (**Supplementary Figure S1D**). This was primarily driven by high SNAI2 expression in resistant PDX (one of the top overexpressed genes in DE analysis). Enrichment of this set indicates enhanced beta-catenin expression/activity in inherently resistant PDX. While inherent radiation resistance has importance, acquired (or adaptive) radiation resistance is the more pressing clinical problem for GBM. Therefore, we sought to develop adaptive radiation resistant models. Eleven PDXs (Radiation Therapy Unselected or RTU) underwent serial in vivo

selection (6-8 serial passages) against radiation therapy (**Figure 1B**). Three of these lines were consistently "cured" by radiation therapy and were thus unable to complete the radiation selection process. However, **Figure 1C** shows the difference in doubling time as combined endpoint probabilities of the remaining sensitive, RTU lines (solid, blue line) and their paired resistant (Radiation Therapy Selected or RTS) lines (dashed red line). The median endpoint probability for the doubling time of the combined RTU lines was reduced by 85% compared to the median of the RTS lines from 35 to 5 days ($p < 0.001$). Eight PDXs were successfully selected for resistance to radiation with parent and selected tumor doubling times as indicated **(Figure 1D)**. Basic clinical demographic information for these lines (**Figure 1E**) and a GBM hallmark driver gene panel (**Figure 1F**) are shown. Of note, CDKN2A/B were deeply deleted in most samples and JX39P and JX39P-RTS harbor the $EGFR_{VIII}$ variant.

Chromosome 12q14 amplification identified in some RTS PDX

Single Nucleotide Polymorphism (SNP) analyses indicated that RTS PDX lines correlated highly with their parent RTU line (**Figure 2A**). Like the GBM hallmark driver gene panel data, these results suggest that RTS PDX lines mirror clinical datasets (14) by generally maintaining their classic genomic alterations. However, two of the eight RTS lines, X1153-RTS and JX14P-RTS, were found to have a copy-number amplification on chromosome 12q14, (**Figure 2B and C**) a locus previously identified in recurrent GBM patients. While 12q amplification could suggest a possible mechanism for the acquired radiation resistance in the RTS lines, we anticipated that transcriptome and kinome assessment may be more revealing.

Transcriptomic analysis identifies differentially regulated lncRNAs that may have functional roles

Intracranial orthotopic xenografts were established and tumors were harvested in biological triplicate for 'omics' analysis (32). Each orthotopic tumor was divided in half for matched kinomic and transcriptomic evaluation. Globally, at the transcriptome level, PDX pairs primarily separated based on patient of origin with some smaller separation based on radiation sensitivity on principal component analysis (**Figure 3A**). Global differential expression (DE) including patient tumor of origin and selection status (~PDX_ID + RTS) revealed 482 significantly differentially expressed genes (DEGs) (**Figure 3B**) including 69 lncRNAs and 24 pseudogenes. Global DE between the combined RTU vs RTS (~RTS), without patient tumor of origin as a covariate, revealed 27 significantly DEGs (**Figure 3C**) including 5 lncRNAs and 1 pseudogene. One of these lncRNAs, CASC19/PCAT2 (ENSG00000254166.3), is globally upregulated in selected PDX (p.adjust = 0.02) (**Supplementary Fig S2A**), particularly in JX39P, and has predicted DNA binding at several genomic sites (method described in **Supplementary Figure S2B**), including sites proximal to mitogen-activated protein kinase 6 (MAP2K6); another globally DEG, and sites on the FES proto-oncogene. In the JX39P pair, CASC19 expression is positively correlated with expression of MAP2K6 and FES (**Supplementary Figure S2C**). Additional differential expression analytic approaches were performed including two machine learning (ML) methods (FastEMC and WGCNA) and differential gene correlation analysis (DGCA) that both identified several lncRNA and pseudogenes being differentially expressed in RTS models that were used for lncRNA correlations (**Supplementary Figure S3**).

To elucidate potential regulatory roles of the differentially expressed lncRNAs, a novel pipeline incorporated RNA:RNA (ASSA) and RNA:DNA (Triplexator) binding prediction software (20, 21) with bedtools to identify proximal genes to lncRNA:DNA binding sites (**Supplementary Figure S2B**). Presumptive cis-regulatory targets for the significantly altered lncRNAs were

identified as genes that were common to both the lncRNA:DNA proximal gene list and the pairwise differentially expressed gene list. Nine lncRNAs were predicted to bind directly to a combined 28 differentially regulated genes identified in upstream analyses (**Figure 3D**). DNA binding potential was discovered for 45 lncRNA at several thousand sites across regulatory regions of the human genome (**Figure 3D**). Some lncRNAs (CASC19/PCAT2, SOX2-OT, ZFAS1, PAQR9-AS1, and USP2-AS1) possessed both RNA:RNA and RNA:DNA binding potential. Searching a 20kb window upstream and downstream from these predicted DNA binding sites, 4,268 proximal genes were discovered (**Figure 3D**). Correlative analysis revealed both strong positive and negative correlations between the expression of lncRNAs and proximal genes (**Supplementary Figure S3** and **Supplementary File S1**). The highest correlated genes were associated with several cancers or cancer related pathways including glioblastoma, astrocytoma, neuroblastoma, leukemia, lymphoma, hepatocellular carcinoma, gastric cancer, stemness, angiogenesis, invasion, proliferation, and DDR (**Supplementary File S1**). Specific pairwise correlations are detailed in the **Supplementary Figure S4** and gene interaction networks (WIPER) are shown in **Supplementary File S2**.

Acquired radiation-resistant tumors display distinct DNA damage repair pathway alterations

One of the hallmarks of radiation resistance is increased or altered DDR activity**. Figs. 4A-F** show the normalized enrichment scores of RTS vs RTU PDX for 12 DDR transcriptional signatures. It was not possible to generate normalized enrichment scores for JX12P, X1465, or X1066 due to the imbalanced number of replicates. Globally, as well as in the JX39P pair, Fanconi anemia (FA), mismatch repair (MMR), nucleotide excision repair (NER), non-

homologous end joining (NHEJ), homologous recombination (HR), and chromatin modification signatures were enriched in RTS PDX (**Figure 4A, 4E**). X1516 also shows similar DDR enrichment to global, except that BER is enriched in RTS PDX with NER conversely decreased (**Figure 4B**). The JX14T pair has similar enrichment to global and JX39P, except that NER and MMR are significantly decreased in the RTS lines (**Figure 4D**). In the X1153 pair, BER, NER, MMR, and FA are enriched in RTS PDX, while HR, NHEJ, and chromatin modification were decreased in RTS PDX (**Figure 4F**). The JX12T pair is the most divergent from the other RTS PDX with all 12 DDR signature normalized enrichment scores decreased for RTS over RTU PDX (**Figure 4C**).

Several lncRNAs showed strong associations with significantly DE DDR genes. In the X1153 pair, AC008764.8 showed a negative correlation with FA-related gene FANCC (**Figure 4F** and **Supplementary Figure S3**). Also, AC124290.1 and AUXG01000058.1 showed strong positive correlations with the HR-related gene SEM1 (**Figure 4F** and **Supplementary Figure S3**). SOX2-OT was positively correlated with NHEJ-related XRCC4 and to a lesser extent with RAD9A (**Supplementary Figure S3**). In the JX39P pair, AC002456.1 was negatively correlated with HR-related RBBP8 (**Figure 4E**) and positively correlated with NER-related MNAT1 and NHEJ-related XRCC5 (**Supplementary Figure S3**).

Kinome profiling identifies PDX-specific actionable targets in RTS PDX

Global kinomic profiling of RTU and RTS pairs revealed common and PDX-specific alterations in kinase signaling. As opposed to global transcriptomic analysis, the kinomic profiles separated PDX primarily by resistance status (RTU or RTS) (**Figure 5A, B**). Globally, kinase signaling was decreased in RTS compared to RTU, when the samples were analyzed together. However, this appeared to be driven by a small subset of samples, such as X1066 and X1516, that had

relatively large kinase activity decreases in RTS compared to RTU (**Supplementary File S3**). Across PDX pairs there was large variation in altered kinase signaling, with some RTS having globally decreased activity in Src family kinase and growth factor pathways (X1066, **Supplementary File S3**), as well as PKC centric decreases (X1516).

Next, upstream kinases alone, and integrated with differentially regulated lncRNA:DNA binding proximal genes, were analyzed at the pathway level (**Supplementary File S4**). Src family kinase activity was upregulated in RTS in the integrated analysis of JX14P and JX39P, while being decreased in X1153 and X1465 RTS. Ephrin receptor activity was increased in RTS variants of JX14P and X1465. We observed increased activity of EGFR and VEGFR signaling in X1153. As we are interested in evaluating pharmaceutical targets, we focus here on those actionable kinases that exhibited increased activity in the RTS PDX.

To test the druggable potential of the kinases increased in **Figure 5C-E** and **Supplementary File S4**, in vitro SMI screening was conducted using sitravatinib and brigatinib in PDX-derived neurosphere cultures. Sitravatinib targets TRKA/B (JX14P-RTS, JX39P-RTS), ROS1 (JX14T-RTS), Src (JX14P-RTS, JX39P-RTS), as well as multiple Ephrin isoforms. Brigatinib targets ROS1 (JX14T-RTS) and the canonical GBM target EGFR (JX39P-RTS). We observed that JX14T-RTS, JX39P-RTS and JX14P -RTS were significantly sensitive to both sitravatinib and brigatinib (**Figure 5F**).

Confirmatory Western blot array analyses were performed using the R&D Systems Proteome Profiler Human Phospho-Kinase Arrays on paired RTU and RTS from JX14P, JX14T, JX39P, and X1465. As shown in **Figure 6A** and **B**, the RTS lines for JX14P, JX14T, and JX39P exhibited increased phosphorylation of multiple kinases and/or kinase targets, including Src family kinases (SFKs) (**Figure 5**). However, X1465-RTS showed phosphorylation decreases or

no appreciable changes compared to its RTU line except for STAT2(Y689) and AKT(S473) which were modestly elevated. These results supported the PamStation Kinomic profiling of X1465-RTS which showed decreased SFK activity relative to its RTU parent (**Supplementary File S4**). Additionally, an upstream kinase comparison was performed to integrate the PamStation kinomic profiles and the R&D Systems based on the Phosphonet database (See **Supplementary Information**). Top increased kinases, validated from the previous kinomic screen, included increased Hck, Yes1, and Src (JX14P-RTS); increased Lyn and Src (JX39P-RTS); and increased JNK2 (X1465-RTS). Across three of the four RTS lines, there were increases in activity of Src-family, PIM-family, MSK1, PYK2, and JNK kinases. Additionally, BRK was activated as the top kinase in JX39P-RTS and scored highly in JX14P-RTS and JX14T-RTS as compared to parental RTU lines (**Supplementary Figure S5**).

Discussion

We generated, characterized, and validated several GBM PDX models of radiation-resistance (RTS) from their radiation sensitive parental (RTU) PDX and identified levels of transcriptomic and phenotypic heterogeneity and mechanisms of acquired resistance. We qualitatively observed a general increase in the invasive potential of orthotopic RTS PDX when dissecting intracranial tumors and quantitatively showed that RTS tumors were more aggressive with significantly reduced overall survival in vivo. We performed genomic, transcriptomic, and functional proteomic (kinomic) testing on these models with results supporting our contention that these models are clinically relevant. Indeed, we found that mutational drivers were generally retained upon radiation selection, a finding previously observed in GBM patients with longitudinal molecular testing (14, 15). When we did detect new amplifications, they tended to be supported by the clinical literature (33), such as the chromosome 12q14 amplification seen in 2 of the 8 RTS pairs. Transcriptomically, the tumor models tended to group based on the tumor of origin rather than RTS status suggesting that acquired radiation resistance may be context dependent. Within individual GBM PDX pairs, however, our transcriptomic analyses suggested several potential pathways to acquired radiation resistance. Additionally, there are RTS mediated differences in the enrichment of a number of GBM-related gene signatures including stemness, cell cycle, chromatin remodeling, IFN-STAT1 signaling, and molecular subtypes.

We observed a contrast in the type of changes from RTU to RTS between global transcriptomic and global kinomic profiling. At the kinome level, samples separated clearly based on radiation selection status and not by patient tumor of origin. This speaks to the downstream, functional-level effects of radiation selection with relatively fewer changes at the transcriptional level. Gross transcription appears to be driven by the inherent genetic background of the original

patient tumor, while the acquired resistance phenotype is functionally distinct at the kinome level. This could suggest that small differences at the transcriptomic level, possibly in lncRNA expression, could have large downstream functional impacts. This is consistent with our knowledge that lncRNAs can have diverse, often concurrent, molecular roles despite their relatively low abundance (17).

We detected both common and PDX-specific differential enrichment of upstream kinases between RTU and RTS PDX. In X1066 and X1516, kinase activity was mostly repressed in RTS PDX, potentially indicating a more homeostatic condition, characteristic of senescent or stem-like cells. In some cases, activities of Src family kinases (JX14P/T, JX39P) and EGFR (X1465, JX39P, JX12T) are increased in RTS PDX. Brigatinib, an anaplastic lymphoma kinase (ALK) and epidermal growth factor receptor (EGFR) inhibitor was effective at killing radiation resistant cells in three selected RTS PDX lines (**Figure 5F**). Sitravatinib, targeting Trk, Src, and Ephrins among others, was also efficacious in these three PDX lines (**Figure 5F**). Of note, brigatinib has demonstrated clinical intracranial efficacy for lung cancer brain metastases, suggesting potential application in recurrent GBM (34). Sitravatinib has been identified as potential therapy for overcoming immune checkpoint blockade resistance (35). As targeting the immune checkpoint blockade has had limited clinical benefit in GBM, it is possible that combining it with drugs such as sitravatinib would be more beneficial. Src and Trk family kinases are induced by radiation treatment in breast cancer cells and in human umbilical vein endothelial cells (HUVEC) (28, 29), while Src has long been considered a therapeutic target in GBM (36). Recently published collaborative work has shown that in vitro radiation-selection of human and murine-derived glioma stem cells (GSCs) can induce IGF1R-mediated resistance pathway via N-cadherin (N-cad) upregulation. IGF1R inhibition could reverse this radiation resistance, which was validated

in two of our RTS lines, JX14P-RTS and JX39P-RTS (11). Together, these suggest that resistance models can be used to identify druggable targets for recurrent, therapy-selected tumors.

RTS PDX models displayed increased in vivo resistance to RT, although there is diversity in the enrichment of DDR signatures (**Figure 4**), indicating potentially different routes to acquired radiation-resistance. Given the high degrees of intra- and intertumoral heterogeneity observed in GBM, it is expected that each individual tumor could adapt differently under therapeutic pressures. Our cohort of selected tumor pairs provides a wide range of molecularly diverse phenotypes for interrogation. Almost universally (excepting JX12T), FA-related DDR was enriched in RTS PDX. The FA core complex of 8 proteins is located in the nucleus and responsible for surveillance for DNA double stranded-breaks (DSB) (37). This complex ubiquitinates FANCD2, which is also phosphorylated by ATM prompting its interaction with the BRCA1/2 complex that also contains RAD51 (38, 39). In this way, FA genes promote DDR primarily through the high fidelity HR pathway (40). The enrichment of the FA-related gene signature may therefore indicate a preferential reliance on this surveillance mechanism in acquired radiation resistance. HR and NHEJ were also frequently enriched in RTS PDX, the exceptions being JX12T and X1153. X1153-RTS PDX appears to rely more on BER, NER, and MMR mechanisms. Interestingly, GSEA using our DDR gene sets revealed an enrichment of 10 out of 12 signatures in inherently resistant tumors, but only NER passed the FDR significance threshold of <0.25. On the whole, differential basal expression, perhaps due to distinct genetic/epigenetic backgrounds, described most of the variance in the model. Radiation resistance status captured a small amount of the variance supporting our thinking that radiation resistance is mediated at a post-transcriptomic/epigenetic level.

Many DDR genes are located proximal to significantly differentially regulated lncRNAs with DNA binding sites in the regulatory genome. Some of these lncRNA:DDR gene associations show positive and/or negative correlations in expression, especially in FA and HR (**Figure 4E**, **4F**, **Supplementary Figure S3**). Our data suggest a relationship between lncRNAs and DDR pathway modulation. It is possible that this is accomplished through epigenetic regulation caused by the direct binding of lncRNAs to regulatory regions of DNA proximal to DDR gene loci.

Our in silico pipeline identified 184 lncRNAs differentially regulated between radiation sensitive RTU and RTS PDX. Some of these; SOX2-OT, ZFAS1, SAMMSON, CASC19/PCAT2, and PVT1 have already been associated with various cancers including gliomas (18, 41, 42). The majority of the lncRNAs identified in this study represent novel transcripts with limited to no known information available about their associations or mechanisms. We evaluated the RNA binding potential of these lncRNA transcripts. Nine lncRNAs had predicted RNA binding capacities with such targets as ZNF154, a putative tumor suppressor in nasopharyngeal carcinoma and prostate cancer (43, 44); JAK3, a tyrosine kinase implicated in leukemias and lymphomas (45, 46); and SOX11, which may act as a tumor promoter or suppressor in various cancers including glioma (47). Forty-five lncRNAs are predicted to bind DNA in regulatory regions of the human genome and have strong correlations with DEGs proximal to those binding sites. We have observed that associations with lncRNA and their potential targets can be either negative or positive, similar to the DDR relationship.

The lncRNA AF106564.1 demonstrated positive correlations with the FIP1L1-PDGFRA fusion transcript and with NTRK3 (**Supplementary File S1**). Fluorescent in situ hybridization using the Vysis LSI 4q12 Tri-Color rearrangement probe was not able to confirm the presence of a canonical deletion in the 4q12 region that leads to the FIP1L1-PDGFRA fusion product in

heterotopic PDX. This is a limitation as the transcript level detection was performed with orthotopic and not with heterotopic PDX, highlighting the differences in molecular signaling dependent on locations of tumor implantation. Amplification of this region may lead to poorer outcomes as PDGFRA is a putative oncogene in glioma and FIP1L1 is constitutively expressed in oligodendrocyte precursor cells (48). The association of AF106564.1 with NTRK3 (ENSG00000140538) is also intriguing as NTRK genes code for tyrosine-kinase receptors for growth factors in the CNS and activating fusions such as ETV6-NTRK3 or BTBD1-NTRK3 have oncogenic potential in some subsets of high-grade glioma (49). Co-expression of these pairs of genes is observed in some of our RTS PDX models. This suggests that lncRNAs may regulate gene fusions, that are a hallmark of many neoplasms.

There are several potential limitations for our study that should be noted. First, radiation therapy selection occurred in a heterotopic tumor location and within immunocompromised (athymic) mice. While prior data suggest that implanting tumors in subcutaneous sites or even culturing in serum-free neural stem cell media and later re-implanting in orthotopic sites does not compromise model fidelity (50, 51), there is concern that subcutaneous selection might impact tumor evolution or restrict tumor diversity. While our RNA-Seq data mapped highly to human suggesting a limited number of murine cells in the bulk sample, we did perform differential gene expression for mouse transcripts and found that mitochondrial genes were significantly decreased in RTS lines compared to the RTU lines (**Supplementary Figure S6**) suggesting that the radiation selection of GBM tumors alters the recruitment of non-tumor stromal cells and that these non-tumor stromal cells are functionally unique from the cells recruited by the parental tumor. Another potential limitation is the lack of detailed patient clinical characteristics for the original tumors used to generate the PDX. Our molecular data, however, suggest that our models

retain diversity and display features that mirror recurrent clinical specimens. Future work will confirm the master regulatory potential of the numerous lncRNA targets that were identified, particularly in their connection with DDR and kinase activation. Moreover, most small molecule inhibitors effectively target multiple kinases. As such, it is unclear the relative contribution of individual kinases identified to the RTS phenotype based on drug treatment alone. Additional studies are needed to pinpoint the key kinase regulators in the RTS tumors, including in vivo experimentation.

To our knowledge, our in vivo RTS GBM PDX models are unique in the field. The differential enrichment in vivo of GBM kinase signaling is recapitulated in vitro, allowing for this model system's versatility in the study of GBM tumor recurrence. Our in silico lncRNA analysis pipeline has identified known and novel lncRNAs associated with therapy resistance. We have presented evidence which links several lncRNAs to DEGs in a variety of differentially regulated, key GBM molecular pathways. Our results are consistent with the known regulatory roles of lncRNAs and may suggest this class of molecules as potential therapeutic targets in the treatment of recurrent, intractable GBM as well as in other cancers. We have also shown that our integrated workflow is able to reveal actionable lncRNA-related pathway targets using SMIs that have efficacy in recurrent, therapy-selected tumors. The combination of these RTS models with matched global kinomic and transcriptomic analysis represents a novel preclinical method for identifying druggable targets in intractable, recurrent GBM tumors.

Methods

PDX generation

PDXs were established from either primary or recurrent GBM surgical specimens, obtained from the Brain Tumor Tissue Core under IRB (X050415007) and IACUC (21435) approval. These PDXs were established by injecting tumor chunks from patient tumors into the flank of athymic nude mice. These tumors were then serially passaged in mice with periodic cryopreservation of tumor chunks at various passages for future cultivation and study. Additional PDXs were acquired from Drs. C.D. James (Northwestern University, Chicago, IL, USA) and J.N. Sarkaria (Mayo Clinic, Rochester, MN, USA) including 4 tumors that are isogenic to 4 of these parental PDXs from Dr. Sarkaria based on selection of temozolomide-resistant tumors from previously temozolomide-sensitive PDXs (52). A total of 20 GBM PDX were initially included in our screenings for this study.

PDX in vivo radiation screening and selection

Radiation screening and selection were performed in heterotopic PDX cultivated in athymic nude mice. Ionizing radiation was delivered using an X-Rad 320 (Precision X-Ray Irradiation, North Branford, CT) and measured using a dosimeter placed in the treatment field. Heterotopically tumor-implanted mice (n=5 per group) were anesthetized and administered 6 fractions of 2 Gy each over a period of two weeks with doses delivered on Monday, Wednesday, and Friday. Radiation administration was initiated when the average tumor volume of the 5 mice was measured to be approximately 200cc. Tumor volume was measured using tissue calipers a minimum of three times per week during and following the treatment period. Tumor volume was calculated using the modified ellipsoid formula ½ (length x width^2) (53, 54). The endpoint of the assay was defined by the time in days it took for the tumor to double in volume from its initial

volume on the first day of irradiation. Tumor doubling time less than 20 days was defined as resistant to therapy and longer than 20 days was sensitive. Tumors which were found to be initially radiation sensitive then underwent serial selection for 6-8 rounds of radiation therapy. The fastest growing tumor from each previous round was harvested and implanted heterotopically into nude mice (n=2) for the subsequent radiation round. Highly sensitive tumors that were "cured" by the standard 12Gy treatment received only 3 X 2Gy fractions for the initial 2 rounds of selection, after which the dosage was returned to the standard course. After the selection rounds were completed, repeat screening with 5 mice per group was performed to confirm the resistant, RTS phenotype.

Orthotopic PDX

Orthotopic PDX were established by stereotactic intracranial injection of 300,000 tumor cells, dissociated from flank tumors, suspended in 5μL of 5% methylcellulose in Dulbecco's MEM

(32). Tumors from control mice were resected and snap frozen in liquid nitrogen for later molecular analysis.

Whole exome sequencing

Genomic DNA was extracted from flash frozen tumors using the Qiagen (Germantown, MD) DNeasy Blood & Tissue Kit (69504). Sequencing libraries were prepared using the Illumina TruSeq DNA Exome kit (20020615), prior to pooling in groups of 12 and sequencing using a Nextseq 550 (Illumina, San Diego, CA) with a NextSeq 500/550 High Output Kit v2.5 (150 Cycles) (20024907) using paired-end settings (2x75).

SNP calls. Raw paired-end exome reads were mapped to a human (hg38) and mouse (mm10) combined reference genome using tophat (version 2.1) which uses bowtie2 (version 2.3.3) as its

underlying short read mapper. Next, an mpileup file was created using bcftools (version 1.6). bcftools was then used to call variants. Vcftools.pl varFilter was then used to filter the calls by sequence read depth (minimum depth 500 nucleotides across all samples). The called SNPs that passed this quality thresholding were then used as input to SNPRelate (version 1.26.0) within R (version 4.1.2). The first 10 principal components were extracted from SNPRelate and were then used to perform multi-dimensional scaling (MDS). A distance matrix was calculated between each sample and a plot was made (using corrplot package version 0.92) with 1-(Euclidean distance) of the MDS plot.

Copy number alteration calls. Raw paired-end exome reads were mapped to a human (hg38) and mouse (mm10) combined reference genome using bowtie2 (version 2.3.3). Next, raw reads were aggregated using patternCNV script bam2wig.sh. PatternCNV pipeline was run per manual with default parameters. Log-2-fold change calls data was extracted from PatternCNV workflow. Data was concatenated and imported into R for data visualization. Exon-level data was summarized by gene using "dplyr" package. "pheatmap" package was used to create a heatmap. In addition, genome-wide plots were visually examined for recurrent large copy-number alterations in the individual RT pairs. Two RTS lines had large chromosome segment amplifications in copy number at chromosome 12q. A zoomed in view of this locus is shown in the parental line and the RTS lines for the two affected PDXs (**Figure 2B**).

RNA Sequencing

Orthotopic tumors were resected from mouse brains, divided into two halves that were placed in sterile screw-cap vials (Sarstedt, Newton , NC), and snap frozen in liquid nitrogen. Samples were stored at -70^{o}C until used. One half of the tumor was used for RNA isolation and the other for

protein lysate. RNA extraction was performed using the Norgen Animal Tissue RNA extraction kit (Norgen, Thorold, ON) following the kit instructions. Snap frozen tissue was first ground into a powder using a mortar and pestle then processed according to the Norgen kit. RNA was quantified using a NanoDrop™ (Thermo Fisher Scientific, Waltham, MA) and 50μg of RNA was sub-aliquoted for RNA sequencing. RNA sequencing was performed by GeneWiz (South Plainfield, NJ). RNA integrity and fragment size were tested using RNA ScreenTape® with average RIN numbers of 8.5 and average fragment length around 4500nt. The samples were then depleted of rRNA before conducting stranded library preparation. Sequencing using biological triplicates for each sample was performed on an Illumina HiSeq 2000 using 150bp PE reads with a median of around 72 million reads per sample. FastQC reports were generated pre-trimming and post-trimming of low-quality bases (Phred score <20) and Illumina adapter sequences using trim-galore-0.4.5. Quasi-mapping and quantification were performed using Salmon-0.12.0 (with --gencode and -k 31 flags for index generation and -l ISR, --gcBias and --validateMappings flags for quantification) against the Gencode GRCh38.p12 release 31 reference transcriptome. A multiQC report was then generated including the use of FastQ Screen (v0.11.2 with dependencies to Bowtie2 v2.3.3 and SAMtools v1.6) to identify the proportions of mouse to human transcripts detected. Three replicates were excluded from further analysis due to high mouse transcript contamination. We retrospectively determined from resection notes that these high mouse content tumors were highly infiltrative and hemorrhagic upon resection. A tx2gene table was then generated from a TxDB object using Bioconductor-genomicfeatures-1.32.3. This table and the quant.sf files from Salmon were then read using tximport (v1.16.1), biomaRt

(v2.44.4), and DESeq2 (v1.28.1) to generate normalized expression tables used in further in silico analysis.

Kinomic analysis

Kinome profiling was performed in the UAB Kinome Core as done previously (55, 56). Another portion of the same snap frozen orthotopic tumor was lysed with pestle grinding for 30min in M-PER™ lysis buffer (Pierce, Rockford, IL) at 4C to extract protein (Bradford assay quantified) for kinomic analysis. Samples (15μg PTK, 2μg STK per array), in biological triplicate, were processed and run on the tyrosine (PTK; 86402 PamChips) or serine/threonine (STK; 97102 PamChips) arrays, testing phosphorylation kinetically against 196 (PTK) or 144 (STK) 12-15 amino-acid substrate targets on the PamStation12 (PamGene, s-Hertogenbosch, The Netherlands). Phosphorylation of peptides was measured over 154 (PTK) or 164 (STK) cycles, with exposures from 10-200ms that were integrated into slopes, multiplied by 100, and Log_2 transformed in BioNavigator (v6.3) (PamGene). Mean peptide phosphorylation per PDX (i.e., mean of replicates) were used for heatmap clustering (unsupervised geometric means-distance), and change per-PDX pair, per-barcode were used for upstream kinase prediction (UpKin PamApp; PTK v6.0, STK v6.0) and for PCA analysis (Shiny PamApp). Kinases with a mean final score (MFS) >2.0 or mean kinases ktatistic (MKS) >5.0 were retained.

In vitro drug response viability assay

PDXs were propagated as neurospheres, cultured in PDX media (DMEM/F12 (50/50 with 2% B27, 20ng/ml EGF, 20ng/ml bFGF, 1% sodium pyruvate, 1% penicillin and streptomycin) similar to our prior reports (57). Neurospheres were dissociated for 20 minutes with Accutase (Innovative Cell Technologies, San Diego, CA) at 37C°, viability-quantified with trypan blue

utilizing the Countess II (ThermoScientific, Waltham, MA), and plated at 500-1500 viable cells per 100 µL for 24h prior to treatment with indicated doses of brigatinib and sitravatinib (Selleckchem, Houston, TX). After 7 days, CellTiter-Glo® (CTG) reagent was added at 20 µl per well for 30 minutes at 37C, prior to reading luminescence on the BioTek Synergy H1 (Winooski, VT). Raw values were corrected to untreated (DMSO) control.

Antibody based phospho-kinase array analysis

PDX cells were maintained in neurobasal media as described previously (57). Cells were lifted from Geltrex with Accutase (Innovative Cell Technologies, San Diego, CA) lysates were collected with supplied reagents and. of phospho-specific protein abundance using R&D Phospho-Kinase Arrays (#ARY003B, R&D Systems, Minneapolis, MN). Cells were collected according to the manufacturers protocol, with protease and phosphatase inhibitors and protein quantified as in the kinomics methods. 300 micrograms of protein were loaded per array, and probed overnight, prior to secondary application for 4h and chemiluminescent development and film scanning. Image analysis was conducted in Image J (v1.53p, NIH) with background removal (rolling ball, 150 pixels, 1200dpi image) prior to image inversion and manual spot selection and intensity quantitation on identical sized regions of interest. All spots were quantified in duplicate. Spots with a mean intensity change of greater than 25% between groups were heatmapped by % change using GraphPad Prism 9.

In silico analysis

The DESeq2 R package was used for normalization, clustering, and DEG. PCAs were performed using the R stats and factoextra packages. DGCA was performed using the DGCA R package

(v1.0.2) with pre-filtering of zero counts and a filter based on empirical Bayes statistics for DEG between RTU and RTS replicates for each sample. The combined normalized expression table and expression table based on pairwise DEG results for each sample were used as an input to FastEMC (v0.0.6) which selected and sorted the genes which best discriminated between the sensitive and resistant phenotype. Normalized expression was in parallel used as the input for the WGCNA R package (v1.69) which selected gene modules that distinguished between and within samples. The modules within samples were analyzed with BEERE to generate interaction networks which were then input in Gene Terrain to visualize the differential utilization of genes within the modules between RTU and RTS PDX. A table of cDNA was converted into FASTA format for lncRNAs and coding genes identified by DEG, DGCA, and FastEMC using the biomaRt package. FASTAs for lncRNAs and coding genes were input into ASSA (v1.00) to identify RNA:RNA predicted interactions. FASTAs for the lncRNA and the Ensembl Regulatory Build (58) were input into Triplexator in order to identify lncRNA:DNA triple helix sites. Triplexator flags –m R,Y,M,P,A; –v -of 0; and –rm 2 were used. Results were filtered to remove any results which contained errors. LncRNA:RNA and lncRNA:DNA binding results were visualized using Circos. BedTools (v2.29.2) was then used to search 20kb upstream and downstream from triple helix sites to identify genes proximal to these potential binding sites. Genes that were both proximal to the lncRNA binding sites and identified as DEGs were considered as purported lncRNA cis-regulatory targets. The R corrr (v0.4.2) package was used to find correlations between the expression of lncRNAs and the proximal genes. Correlations were also calculated for pairwise and global differentially regulated genes that intersected curated gene sets for DDR, stemness, chromatin remodeling, cell cycle progression, among others. Genes of interest from DEG, DGCA, FastEMC, ASSA, and Triplexator/BedTools were then

input into PAGER and GSEA (59, 60) for gene set enrichment analysis. Key terms from PAGER were then combined with the lists of differentially regulated genes as input for BEERE which constructed gene:semantic interaction networks. The intersection of DEGs from each PDX pair with lncRNAs and their proximal genes was used as input to WIPER which identified key gene pair relationships and generated lncRNA:mRNA transcript interaction networks. In parallel, upstream kinomics data was combined with lncRNA proximal genes of interest using MetaCore/GeneGo (Clarivate Analytics, Philadelphia, PA) for integrated pathway analysis.

Inherent radiation resistance analysis

To assess the transcriptomic differences between inherently resistant and sensitive tumors, we performed differential expression analysis between these two groups (n=7 sensitive, n=6 resistant) using Affymetrix array data (Whole Transcript Human Exon 1.0 ST). Data were quantile-normalized together with the downloaded Affymetrix Human Exon 1.0 ST data of the core TCGA samples (61). Data were then summarized into expression levels for each gene using the pipeline described by Lockstone (62). PDX samples were run in triplicate and collapsed using the average expression. The EdgeR and limma R packages were used to perform the differential expression analysis. Samples were grouped into a DGEList object and then normalization factors were calculated. The model used for analysis was ~0+PDX_ID+RT_Status to account for differences in radiation status as well as tumor specific baseline differences. The dispersion was then estimated using the estimateDisp() function. We then tested the differences between inherent resistant and sensitive tumors using the exactTest() function. A Benjamini-Hochberg (BH)-adjusted p-value of 0.05 was used as the significance threshold. Over representation analysis was then performed in WebGestAlt using available GO and pathway

databases. Enrichment analysis was also performed using the Broad GSEA program using the default settings and a combination of MsigDB sets as well as our custom gene sets.

Statistics

P-values for differential expression were calculated using Fisher's exact test and then adjusted using the Benjamini-Hochberg procedure. False discovery rates (FDR) were used for all GSEA, ORA, and PAGER results. In vitro growth assays including comparisons of tumor median doubling times were evaluated for significance using a standard two-tailed student's T-test. Comparisons of Kaplan Meier endpoint-probability traces were made using log-rank tests. P-values <0.05 were considered significant.

Figure preparation

Several figures (1-4, and 6), including the graphical abstract, were created with BioRender.com under their academic license terms.

Data and resource sharing

Data, resources/reagents, software and further information requests should be directed to the Corresponding Author. Whole exome sequencing data can be downloaded using accession number PRJNA847439 (https://www.ncbi.nlm.nih.gov/sra/PRJNA847439). The RNA-Seq data have been deposited in NCBI's Gene Expression Omnibus and are accessible through GEO Series accession number GSE206225 (https://www.ncbi.nlm.nih.gov/geo/query/acc.cgi?acc=GSE206225). Detailed in silico methods are included in the Supplementary Information.

Study and research approval

PDXs were established from either primary or recurrent GBM surgical specimens, obtained from the Brain Tumor Tissue Core under IRB (X050415007) and IACUC (21435) approval.

Author contributions

Conceptualization: CTS, GYG, CDW; Experimental Design: CTS, GYG, CDW; Writing (Primary): CTS; Writing (Editing): JCA, ZY, TN, NJE, CPL, JW, JRR, CX, FMM, ESY, ABH, CRM, XC, JYC, GYG, CDW; Data Collection: CTS, JCA, NJE CX, FMM, ESY, REB, HA; Data Analysis: CTS, JCA, ZY, TN, JW, JRR, KJL, XC, CDW; Funding: ABH, CRM, JYC, GYG, CDW.

Acknowledgements

We would like to thank Lara Ianov, PhD for her assistance in some code and data visualization guidance.

Supplementary files

Supplementary Information: Additional approaches and description, Supplementary Figures S1-S6, and supplementary references

Supplementary File S1: lncRNA/target correlation spreadsheet

Supplementary File S2: WIPER network analysis

Supplementary File S3: Pairwise upstream kinase predictions

Supplementary File S4: Kinomic and transcriptomic integrated pathway analysis

References

1. von Rosenstiel C, Wiestler B, Haller B, Schmidt-Graf F, Gempt J, Bettstetter M, et al. Correlation of the quantitative level of MGMT promoter methylation and overall survival in primary diagnosed glioblastomas using the quantitative MethyQESD method. *J Clin Pathol.* 2020;73(2):112-5.
2. Stupp R, Mason WP, van den Bent MJ, Weller M, Fisher B, Taphoorn MJ, et al. Radiotherapy plus concomitant and adjuvant temozolomide for glioblastoma. *N Engl J Med.* 2005;352(10):987-96.
3. Hegi ME, Diserens AC, Gorlia T, Hamou MF, de Tribolet N, Weller M, et al. MGMT gene silencing and benefit from temozolomide in glioblastoma. *N Engl J Med.* 2005;352(10):997-1003.
4. Szopa W, Burley TA, Kramer-Marek G, and Kaspera W. Diagnostic and Therapeutic Biomarkers in Glioblastoma: Current Status and Future Perspectives. *BioMed research international.* 2017;2017:8013575.
5. Tang Z, Dokic I, Knoll M, Ciamarone F, Schwager C, Klein C, et al. Radioresistance and Transcriptional Reprograming of Invasive Glioblastoma Cells. *Int J Radiat Oncol Biol Phys.* 2022;112(2):499-513.
6. Wu Q, Berglund AE, and Etame AB. The Impact of Epigenetic Modifications on Adaptive Resistance Evolution in Glioblastoma. *International journal of molecular sciences.* 2021;22(15):8324.
7. Nicholson JG, and Fine HA. Diffuse Glioma Heterogeneity and Its Therapeutic Implications. *Cancer discovery.* 2021;11(3):575-90.
8. Berg TJ, Marques C, Pantazopoulou V, Johansson E, von Stedingk K, Lindgren D, et al. The Irradiated Brain Microenvironment Supports Glioma Stemness and Survival via Astrocyte-Derived Transglutaminase 2. *Cancer Res.* 2021;81(8):2101-15.
9. Fletcher-Sananikone E, Kanji S, Tomimatsu N, Di Cristofaro LFM, Kollipara RK, Saha D, et al. Elimination of Radiation-Induced Senescence in the Brain Tumor Microenvironment Attenuates Glioblastoma Recurrence. *Cancer Res.* 2021;81(23):5935-47.
10. Kang H, Lee S, Kim K, Jeon J, Kang SG, Youn H, et al. Downregulated CLIP3 induces radioresistance by enhancing stemness and glycolytic flux in glioblastoma. *J Exp Clin Cancer Res.* 2021;40(1):282.
11. Osuka S, Zhu D, Zhang Z, Li C, Stackhouse CT, Sampetrean O, et al. N-cadherin upregulation mediates adaptive radioresistance in glioblastoma. *J Clin Invest.* 2021;131(6).
12. Stackhouse CT, Gillespie GY, and Willey CD. Cancer Explant Models. *Curr Top Microbiol Immunol.* 2021;430:131-60.
13. Biau J, Chautard E, De Koning L, Court F, Pereira B, Verrelle P, et al. Predictive biomarkers of resistance to hypofractionated radiotherapy in high grade glioma. *Radiat Oncol.* 2017;12(1):123.
14. Barthel FP, Johnson KC, Varn FS, Moskalik AD, Tanner G, Kocakavuk E, et al. Longitudinal molecular trajectories of diffuse glioma in adults. *Nature.* 2019;576(7785):112-20.

15. Korber V, Yang J, Barah P, Wu Y, Stichel D, Gu Z, et al. Evolutionary Trajectories of IDH(WT) Glioblastomas Reveal a Common Path of Early Tumorigenesis Instigated Years ahead of Initial Diagnosis. *Cancer Cell.* 2019;35(4):692-704 e12.
16. Bhat SA, Ahmad SM, Mumtaz PT, Malik AA, Dar MA, Urwat U, et al. Long non-coding RNAs: Mechanism of action and functional utility. *Noncoding RNA Res.* 2016;1(1):43-50.
17. Stackhouse CT, Gillespie GY, and Willey CD. Exploring the Roles of lncRNAs in GBM Pathophysiology and Their Therapeutic Potential. *Cells.* 2020;9(11).
18. Carlevaro-Fita J, Lanzós A, Feuerbach L, Hong C, Mas-Ponte D, Pedersen JS, et al. Cancer LncRNA Census reveals evidence for deep functional conservation of long noncoding RNAs in tumorigenesis. *Communications Biology.* 2020;3(1):56.
19. Patro R, Duggal G, Love MI, Irizarry RA, and Kingsford C. Salmon provides fast and bias-aware quantification of transcript expression. *Nat Methods.* 2017;14(4):417-9.
20. Antonov I, Marakhonov A, Zamkova M, and Medvedeva Y. ASSA: Fast identification of statistically significant interactions between long RNAs. *J Bioinform Comput Biol.* 2018;16(1):1840001.
21. Buske FA, Bauer DC, Mattick JS, and Bailey TL. Triplexator: detecting nucleic acid triple helices in genomic and transcriptomic data. *Genome Res.* 2012;22(7):1372-81.
22. McKenzie AT, Katsyv I, Song WM, Wang M, and Zhang B. DGCA: A comprehensive R package for Differential Gene Correlation Analysis. *BMC Syst Biol.* 2016;10(1):106.
23. Langfelder P, and Horvath S. WGCNA: an R package for weighted correlation network analysis. *BMC bioinformatics.* 2008;9:559.
24. Stackhouse CT, Rowland JR, Shevin RS, Singh R, Gillespie GY, and Willey CD. A Novel Assay for Profiling GBM Cancer Model Heterogeneity and Drug Screening. *Cells.* 2019;8(7).
25. Yue Z, Kshirsagar MM, Nguyen T, Suphavilai C, Neylon MT, Zhu L, et al. *Bioinformatics*. 2015:i250-7.
26. Yue Z, Willey CD, Hjelmeland AB, and Chen JY. BEERE: a web server for biomedical entity expansion, ranking and explorations. *Nucleic Acids Res.* 2019;47(W1):W578-W86.
27. Bhullar KS, Lagaron NO, McGowan EM, Parmar I, Jha A, Hubbard BP, et al. Kinase-targeted cancer therapies: progress, challenges and future directions. *Mol Cancer.* 2018;17(1):48.
28. Kim RK, Cui YH, Yoo KC, Kim IG, Lee M, Choi YH, et al. Radiation promotes malignant phenotypes through SRC in breast cancer cells. *Cancer Sci.* 2015;106(1):78-85.
29. Jarboe JS, Jaboin JJ, Anderson JC, Nowsheen S, Stanley JA, Naji F, et al. Kinomic profiling approach identifies Trk as a novel radiation modulator. *Radiother Oncol.* 2012;103(3):380-7.
30. Dolan M, Mastri M, Tracz A, Christensen JG, Chatta G, and Ebos JML. *PLoS One*. 2019.
31. Camidge DR, Kim DW, Tiseo M, Langer CJ, Ahn MJ, Shaw AT, et al. Exploratory Analysis of Brigatinib Activity in Patients With Anaplastic Lymphoma Kinase-Positive Non-Small-Cell Lung Cancer and Brain Metastases in Two Clinical Trials. *J Clin Oncol.* 2018;36(26):2693-701.
32. Giannini C, Sarkaria JN, Saito A, Uhm JH, Galanis E, Carlson BL, et al. Patient tumor EGFR and PDGFRA gene amplifications retained in an invasive intracranial xenograft model of glioblastoma multiforme. *Neuro Oncol.* 2005;7(2):164-76.

33. Fischer U, Leidinger P, Keller A, Folarin A, Ketter R, Graf N, et al. Amplicons on chromosome 12q13-21 in glioblastoma recurrences. *Int J Cancer.* 2010;126(11):2594-602.
34. Huber RM, Hansen KH, Paz-Ares Rodriguez L, West HL, Reckamp KL, Leighl NB, et al. Brigatinib in Crizotinib-Refractory ALK+ NSCLC: 2-Year Follow-up on Systemic and Intracranial Outcomes in the Phase 2 ALTA Trial. *Journal of thoracic oncology : official publication of the International Association for the Study of Lung Cancer.* 2020;15(3):404-15.
35. Du W, Huang H, Sorrelle N, and Brekken RA. Sitravatinib potentiates immune checkpoint blockade in refractory cancer models. *JCI Insight.* 2018;3(21).
36. Kenchappa RS, Liu Y, Argenziano MG, Banu MA, Mladek AC, West R, et al. Protein kinase Ciota and SRC signaling define reciprocally related subgroups of glioblastoma with distinct therapeutic vulnerabilities. *Cell reports.* 2021;37(8):110054.
37. D'Andrea AD. Susceptibility pathways in Fanconi's anemia and breast cancer. *N Engl J Med.* 2010;362(20):1909-19.
38. Castillo P, Bogliolo M, and Surralles J. Coordinated action of the Fanconi anemia and ataxia telangiectasia pathways in response to oxidative damage. *DNA Repair (Amst).* 2011;10(5):518-25.
39. Sobeck A, Stone S, Landais I, de Graaf B, and Hoatlin ME. *J Biol Chem*. 2009:25560-8.
40. Chun J, Buechelmaier ES, and Powell SN. *Mol Cell Biol*. 2013:387-95.
41. Onagoruwa OT, Pal G, Ochu C, and Ogunwobi OO. Oncogenic Role of PVT1 and Therapeutic Implications. *Frontiers in oncology.* 2020;10:17.
42. Wang XD, Lu J, Lin YS, Gao C, and Qi F. Functional role of long non-coding RNA CASC19/miR-140-5p/CEMIP axis in colorectal cancer progression in vitro. *World J Gastroenterol.* 2019;25(14):1697-714.
43. Hu Y, Qi MF, Xu QL, Kong XY, Cai R, Chen QQ, et al. *Oncotarget*. 2017:85749-58.
44. Zhang W, Shu P, Wang S, Song J, Liu K, Wang C, et al. ZNF154 is a promising diagnosis biomarker and predicts biochemical recurrence in prostate cancer. *Gene.* 2018;675:136-43.
45. Jeong EG, Kim MS, Nam HK, Min CK, Lee S, Chung YJ, et al. Somatic mutations of JAK1 and JAK3 in acute leukemias and solid cancers. *Clin Cancer Res.* 2008;14(12):3716-21.
46. Nairismägi ML, Gerritsen ME, Li ZM, Wijaya GC, Chia BKH, Laurensia Y, et al. *Leukemia*. 2018:1147-56.
47. Yang Z, Jiang S, Lu C, Ji T, Yang W, Li T, et al. *Therapeutic advances in medical oncology*. 2019:1758835919853449.
48. Sturm D, Bender S, Jones DT, Lichter P, Grill J, Becher O, et al. Paediatric and adult glioblastoma: multiform (epi)genomic culprits emerge. *Nat Rev Cancer.* 2014;14(2):92-107.
49. Gambella A, Senetta R, Collemi G, Vallero SG, Monticelli M, Cofano F, et al. NTRK Fusions in Central Nervous System Tumors: A Rare, but Worthy Target. *International journal of molecular sciences.* 2020;21(3).
50. Haddad AF, Young JS, Amara D, Berger MS, Raleigh DR, Aghi MK, et al. Mouse models of glioblastoma for the evaluation of novel therapeutic strategies. *Neurooncol Adv.* 2021;3(1):vdab100.

51. Jacob F, Salinas RD, Zhang DY, Nguyen PTT, Schnoll JG, Wong SZH, et al. A Patient-Derived Glioblastoma Organoid Model and Biobank Recapitulates Inter- and Intra-tumoral Heterogeneity. *Cell.* 2020;180(1):188-204 e22.
52. Kitange GJ, Mladek AC, Carlson BL, Schroeder MA, Pokorny JL, Cen L, et al. Inhibition of histone deacetylation potentiates the evolution of acquired temozolomide resistance linked to MGMT upregulation in glioblastoma xenografts. *Clin Cancer Res.* 2012;18(15):4070-9.
53. Euhus DM, Hudd C, LaRegina MC, and Johnson FE. Tumor measurement in the nude mouse. *J Surg Oncol.* 1986;31(4):229-34.
54. Tomayko MM, and Reynolds CP. Determination of subcutaneous tumor size in athymic (nude) mice. *Cancer Chemother Pharmacol.* 1989;24(3):148-54.
55. Chandrashekar DS, Chakravarthi B, Robinson AD, Anderson JC, Agarwal S, Balasubramanya SAH, et al. Therapeutically actionable PAK4 is amplified, overexpressed, and involved in bladder cancer progression. *Oncogene.* 2020;39(20):4077-91.
56. Ibrahim AN, Yamashita D, Anderson JC, Abdelrashid M, Alwakeal A, Estevez-Ordonez D, et al. Intratumoral spatial heterogeneity of BTK kinomic activity dictates distinct therapeutic response within a single glioblastoma tumor. *J Neurosurg.* 2019;133(6):1-12.
57. Eustace NJ, Anderson JC, Warram JM, Widden HN, Pedersen RT, Alrefai H, et al. A cell-penetrating MARCKS mimetic selectively triggers cytolytic death in glioblastoma. *Oncogene.* 2020;39(46):6961-74.
58. Zerbino DR, Wilder SP, Johnson N, Juettemann T, and Flicek PR. The ensembl regulatory build. *Genome biology.* 2015;16:56.
59. Mootha VK, Lindgren CM, Eriksson KF, Subramanian A, Sihag S, Lehar J, et al. PGC-1alpha-responsive genes involved in oxidative phosphorylation are coordinately downregulated in human diabetes. *Nature genetics.* 2003;34(3):267-73.
60. Subramanian A, Tamayo P, Mootha VK, Mukherjee S, Ebert BL, Gillette MA, et al. Gene set enrichment analysis: A knowledge-based approach for interpreting genome-wide expression profiles. *Proceedings of the National Academy of Sciences.* 2005;102(43):15545-50.
61. Verhaak RG, Hoadley KA, Purdom E, Wang V, Qi Y, Wilkerson MD, et al. Integrated genomic analysis identifies clinically relevant subtypes of glioblastoma characterized by abnormalities in PDGFRA, IDH1, EGFR, and NF1. *Cancer Cell.* 2010;17(1):98-110.
62. Lockstone HE. Exon array data analysis using Affymetrix power tools and R statistical software. *Brief Bioinform.* 2011;12(6):634-44.

A

GBM-X ID	Radiation Status	Median Doubling Time (Days)
JX59T	Sensitive	90
X1153	Sensitive	60
X1016	Sensitive	55
X1524	Sensitive	54
JX14T	Sensitive	50.5
JX39P	Sensitive	43
X1066	Sensitive	36.5
JX14P	Sensitive	31
JX12T	Sensitive	30
X1465	Sensitive	24
X1238	Intermediate	20
X1516	Intermediate	19
JX22P	Resistant	12
X1046	Resistant	9
X1441	Resistant	7
JX59P	Resistant	7
X1052	Resistant	7
JX39T	Resistant	7
JX12P	Resistant	4
JX22T	Resistant	4

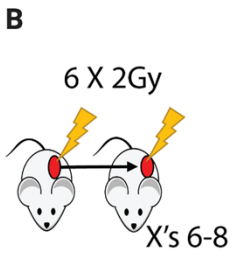

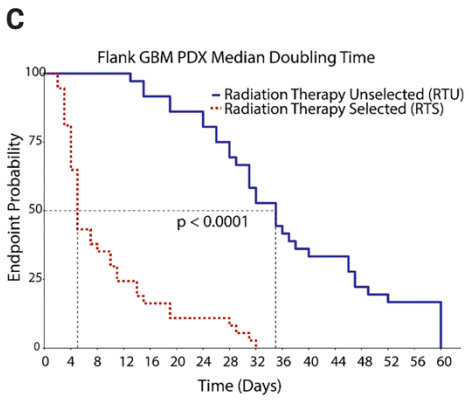

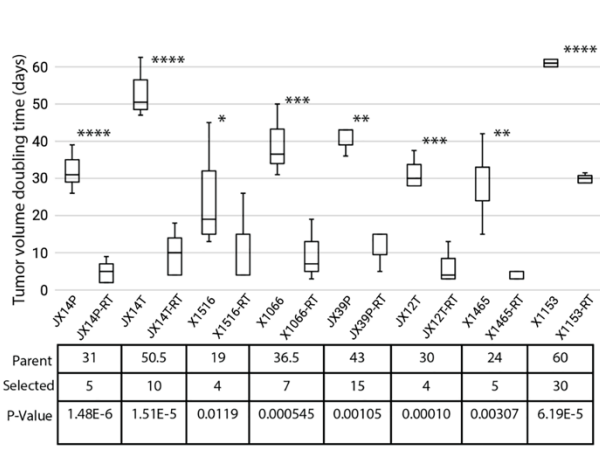

	JX14P	JX14P-RT	JX14T	JX14T-RT	X1516	X1516-RT	X1066	X1066-RT	JX39P	JX39P-RT	JX12T	JX12T-RT	X1465	X1465-RT	X1153	X1153-RT
Parent	31		50.5		19		36.5		43		30		24		60	
Selected	5		10		4		7		15		4		5		30	
P-Value	1.48E-6		1.51E-5		0.0119		0.000545		0.00105		0.00010		0.00307		6.19E-5	

E

PDX-ID	Median IC Survival (Days)		Gender	Age at Diagnosis	Source
	Parent (RTU)	*-RT (RTS)*			
JX12T	26 ± 1.2	25 ± 3.1	M	68	Mayo
JX14P	46 ± 1.8	60.5 ± 4.1	M	58	Mayo
JX14T	51 ± 1.1	24 ± 4.5	M	58	Mayo
JX39P	19 ± 1.8	17 ± 1.0	M	51	Mayo
X1066	25.5 ± 6.2	23.5 ± 2.3	F	64	UAB
X1153	56.5 ± 4.6	59 ± 8.4	F	56	UAB
X1465	50 ± 6.4	37.5 ± 4.0	F	68	UAB
X1516	71 ± 5.2	92 ± 2.3	F	48	UAB

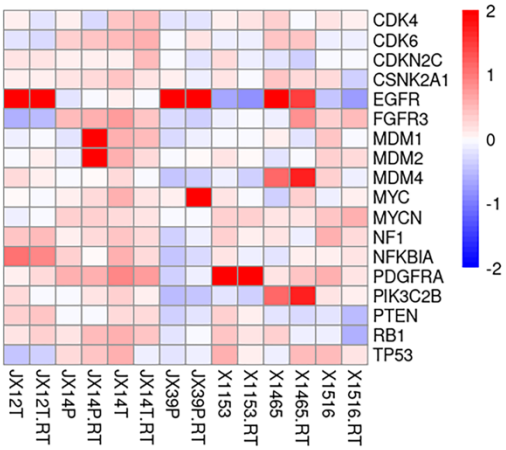

Figure 1. GBM PDX RT-selected models exhibit differences in survival and molecular diversity. (**A**) Initial RT sensitivity status and median doubling times for tumors post RT. (**B**) serial in vivo RT selection methodology. (**C**) RTS (red, dashed line) and RTU (blue, solid line) combined endpoint probabilities following initiation of radiation treatment. P-value calculated from log-rank test. (**D**) changes in median doubling time pre- and post-RT selection. P-values calculated by two-sided student's t-test. E, Basic characteristics of PDX used for RTS with gender (M=male, F=Female), patient age, and original source. F, Log-2-fold change copy number calls from PatternCNV for GBM hallmark genes. Median survival IC (n=6). Median doubling time (n=5).

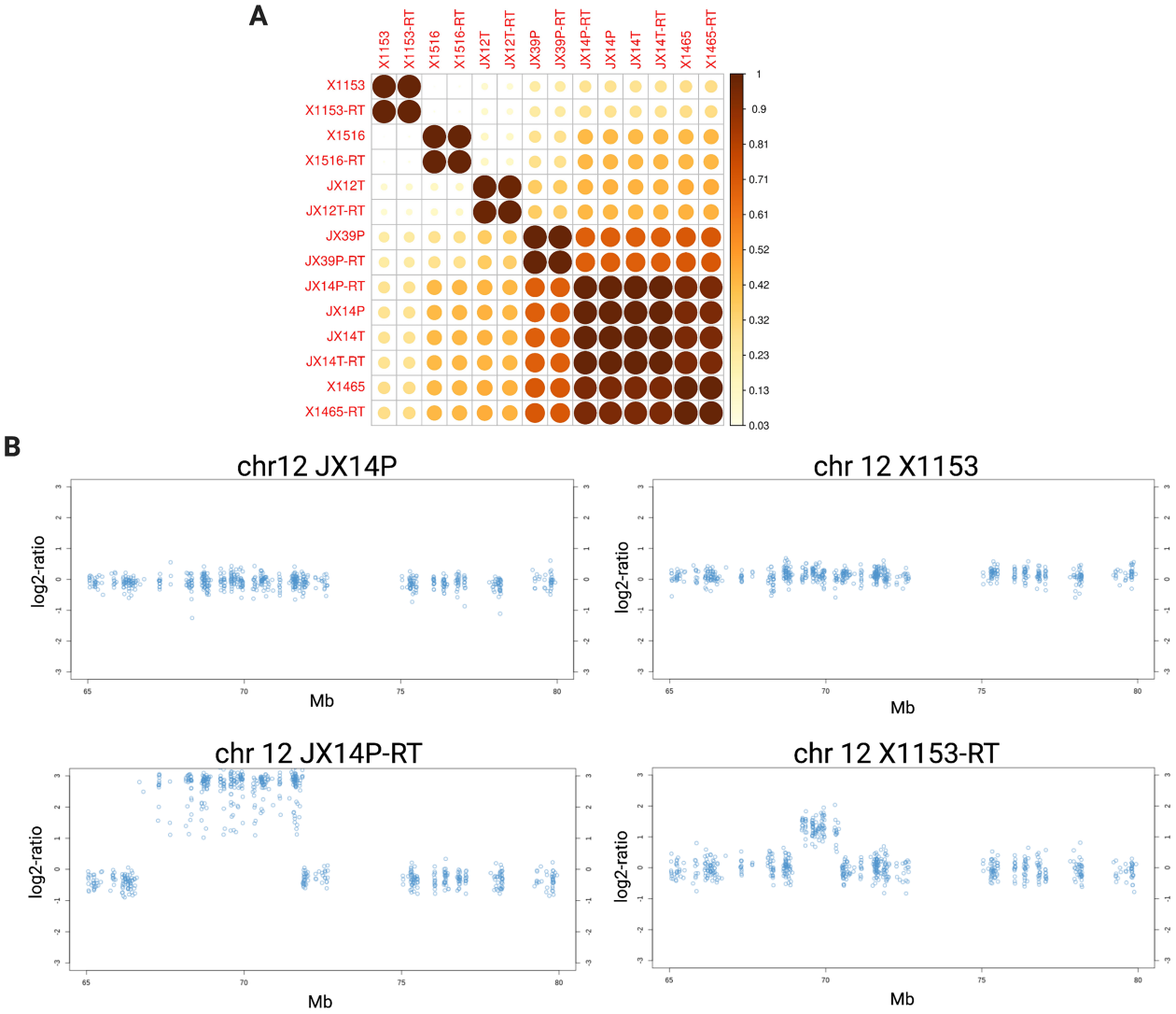

Figure 2. Identification of chromosome 12q14 amplification in select GBM PDX-RT models. (**A**) Multi-dimensional scaling (MDS) of SNP correlations from whole exome sequencing data. A distance matrix was calculated between each sample and a corrplot was made with 1-(Euclidean distance) of the MDS plot. (**B**) PatternCNV output zoomed in view for amplification locus in chromosome 12q for JX14P and JX14P-RT (left panel) and X1153 and X1153-RT (right panel).

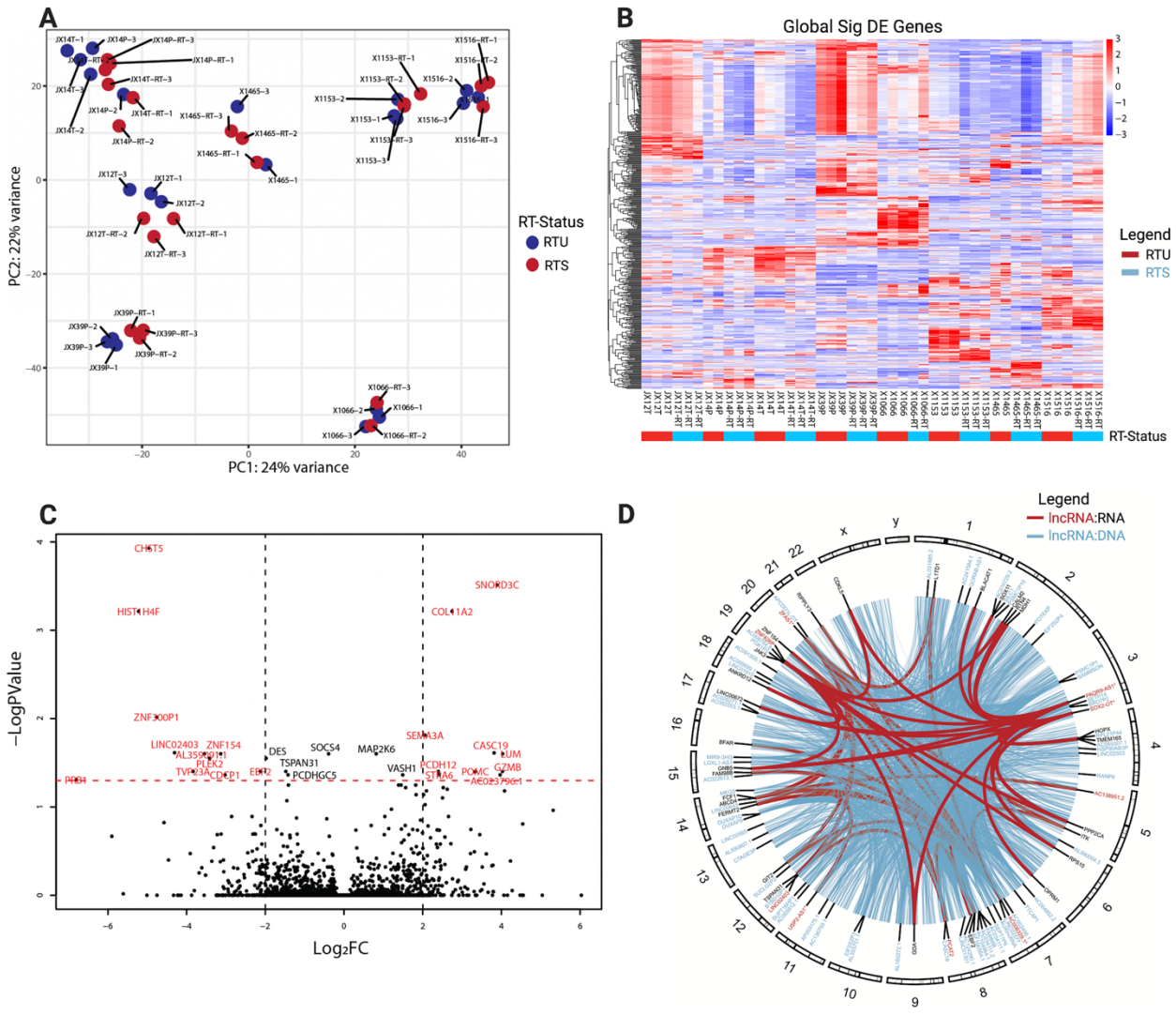

Figure 3. GBM PDX grossly separate according to patient tumor of origin with a small number of significantly DEGs between RTU and RTS. (**A**) PCA of global transcriptomic differences. (**B**) Heatmap of globally DEGs when modeled as ~ PDX_ID + RTS. (**C**) Volcano plot of globally DEGs when modeled by ~ RTS alone (Red text meet cutoffs of log2 fold change >2, <-2, adjusted p-value <0.05). (**D**) Circos plot of differentially regulated lncRNAs (red) with their direct DNA-binding targets (black) and differentially regulated lncRNAs (blue) with their DNA binding sites.

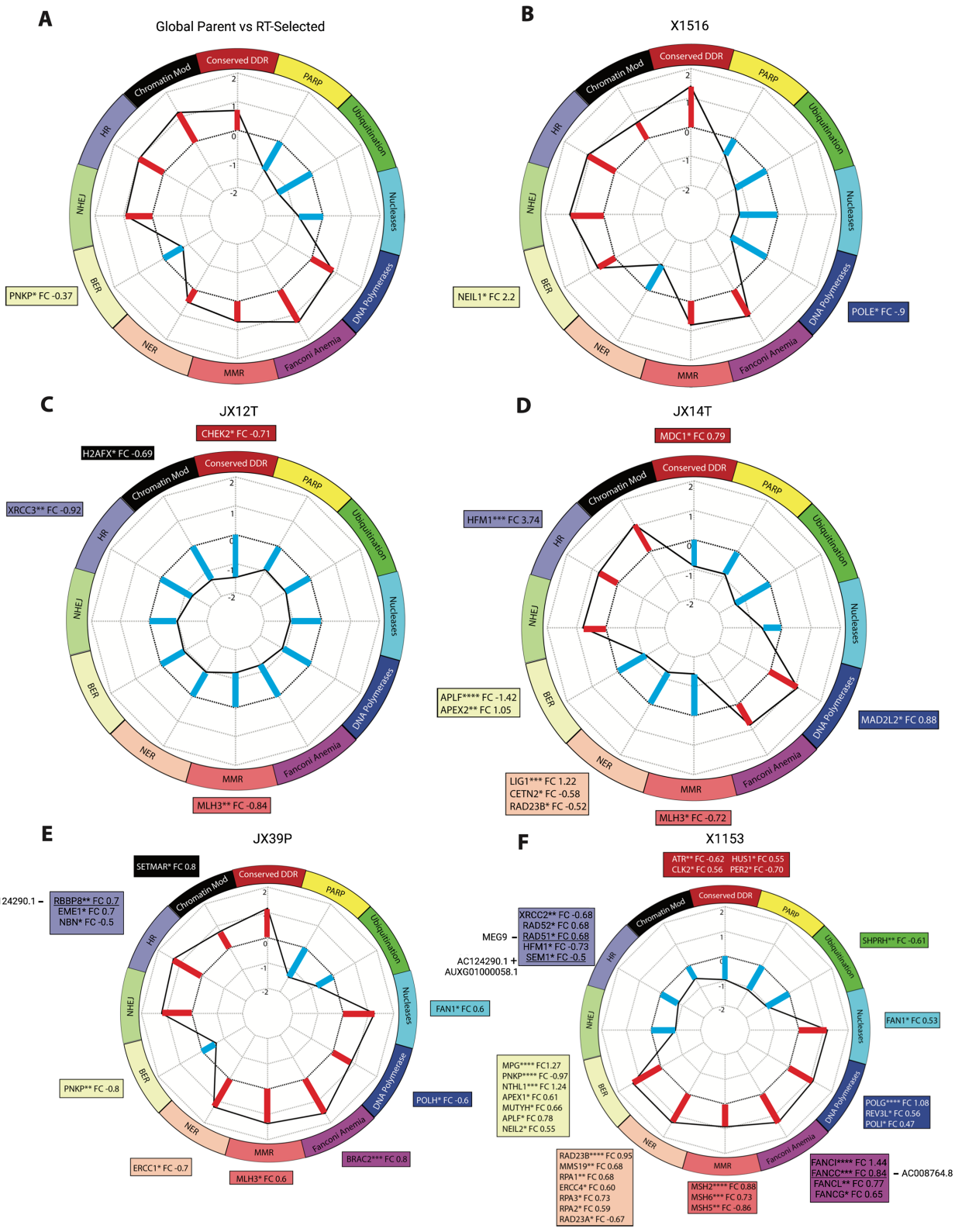
A
Global Parent vs RT-Selected
Conserved DDR
PARP
Ubiquitination
Nucleases
DNA Polymerases
Fanconi Anemia
MMR
NER
BER
NHEJ
HR
Chromatin Mod
PNKP* FC -0.37
B
X1516
NEIL1* FC 2.2
POLE* FC -.9
C
JX12T
CHEK2* FC -0.71
H2AFX* FC -0.69
XRCC3** FC -0.92
MLH3** FC -0.84
D
JX14T
MDC1* FC 0.79
HFM1*** FC 3.74
APLF**** FC -1.42
APEX2** FC 1.05
MAD2L2* FC 0.88
LIG1*** FC 1.22
CETN2* FC -0.58
RAD23B* FC -0.52
MLH3* FC -0.72
E
JX39P
SETMAR* FC 0.8
AC124290.1 –
RBBP8** FC 0.7
EME1* FC 0.7
NBN* FC -0.5
FAN1* FC 0.6
PNKP** FC -0.8
POLH* FC -0.6
ERCC1* FC -0.7
MLH3* FC 0.6
BRAC2*** FC 0.8
F
X1153
ATR** FC -0.62
HUS1* FC 0.55
CLK2* FC 0.56
PER2* FC -0.70
MEG9 –
XRCC2** FC -0.68
RAD52* FC 0.68
RAD51* FC 0.68
HFM1* FC -0.73
SEM1* FC -0.5
AC124290.1 +
AUXG01000058.1
SHPRH** FC -0.61
FAN1* FC 0.53
MPG**** FC1.27
PNKP**** FC -0.97
NTHL1*** FC 1.24
APEX1* FC 0.61
MUTYH* FC 0.66
APLF* FC 0.78
NEIL2* FC 0.55
POLG**** FC 1.08
REV3L* FC 0.56
POLI* FC 0.47
RAD23B**** FC 0.95
MMS19** FC 0.68
RPA1** FC 0.68
ERCC4* FC 0.60
RPA3* FC 0.73
RPA2* FC 0.59
RAD23A* FC -0.67
MSH2**** FC 0.88
MSH6*** FC 0.73
MSH5** FC -0.86
FANCI**** FC 1.44
FANCC*** FC 0.84
FANCL** FC 0.77
FANCG* FC 0.65
– AC008764.8

Figure 4. Differential enrichment of DDR pathways and response to DNA damage in PDX pairs. Enrichment of DDR pathways in RTS globally (**A**), in X1516 (**B**), in JX12T (**C**), in JX14T (**D**), in JX39P (**E**), and in X1153 (**F**). The outside edge of the radar plot is labeled and color coded by DDR pathway. Lines and bars within the plot indicate the normalized enrichment score (-2 to 2) for each DDR signature. Red bars indicate enrichment in the RTS PDX and blue bars indicate enrichment in the RTU PDX. Significantly DEGs within each pathway along with their significance level and log2 fold change (FC) are listed in the boxes color coded to match the DDR pathways in the radar plot. P-values for differential expression are from Fisher's exact test. Underlines genes are correlated with the expression of lncRNAs which are labeled next to the DDR gene. (+) indicates a positive correlation with expression and (-) indicates a negative correlation. HR: homologous recombination, NHEJ: non-homologous end-joining, BER: base excision repair, NER: nucleotide excision repair, MMR: mismatch repair.

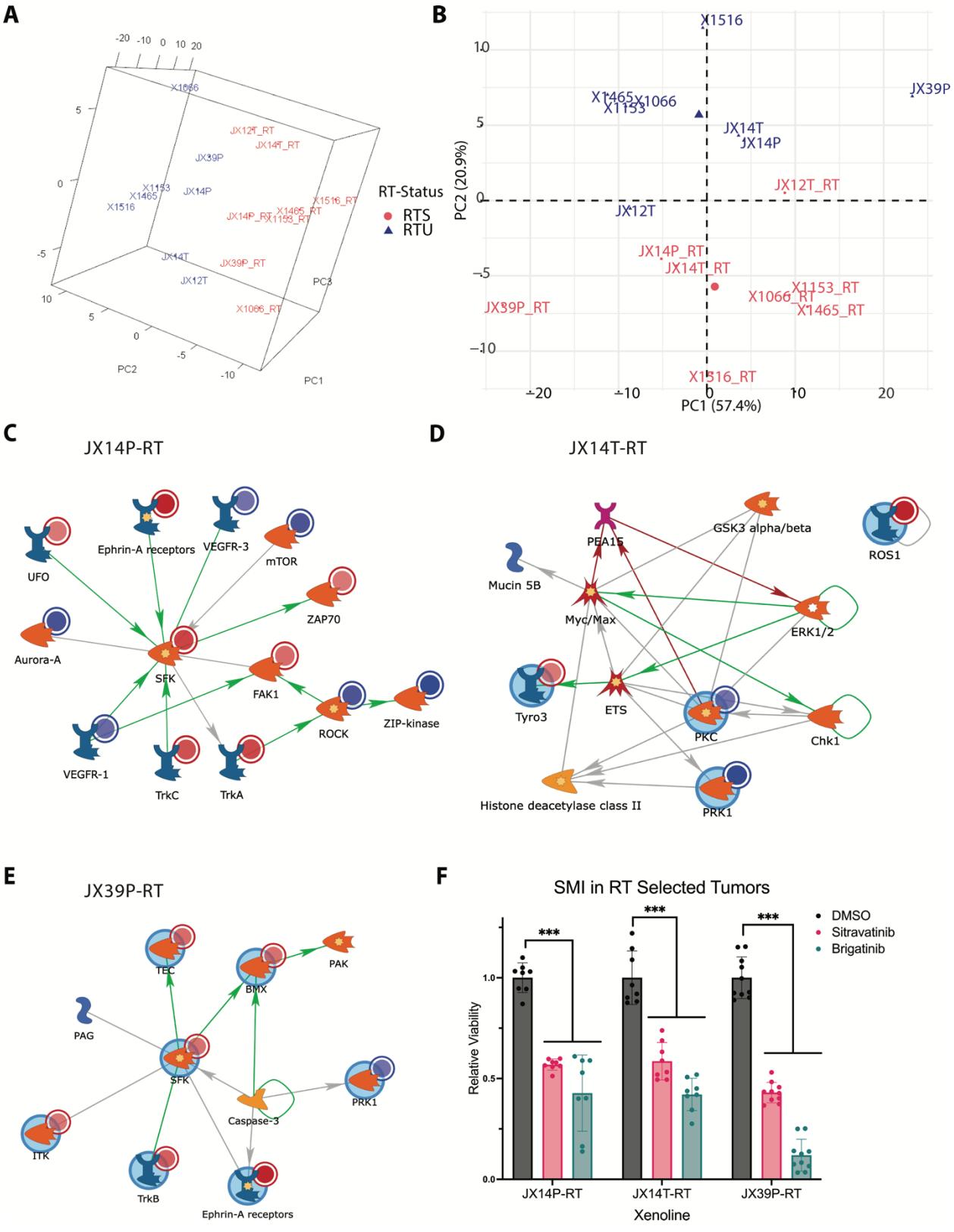
A
RT-Status
RTS
RTU
PC1
PC2
PC3
B
PC1 (57.4%)
PC2 (20.9%)
C
JX14P-RT
UFO
Ephrin-A receptors
VEGFR-3
mTOR
ZAP70
Aurora-A
SFK
FAK1
ZIP-kinase
ROCK
VEGFR-1
TrkC
TrkA
D
JX14T-RT
PEA15
GSK3 alpha/beta
ROS1
Mucin 5B
Myc/Max
ERK1/2
Tyro3
ETS
PKC
Chk1
Histone deacetylase class II
PRK1
E
JX39P-RT
TEC
BMX
PAK
PAG
SFK
PRK1
Caspase-3
ITK
TrkB
Ephrin-A receptors
F
SMI in RT Selected Tumors
DMSO
Sitravatinib
Brigatinib
Relative Viability
JX14P-RT
JX14T-RT
JX39P-RT
Xenoline

Figure 5. Kinase signaling alterations in RTS targeted with SMIs. Principal component analysis demonstrates separation of kinomic signal signatures across 3 components (**A**), colored by RTS (red) and RTU (blue) with the 1st 2 components plotted in (**B**). Kinases altered in RTS compared to RTU for JX14P (**C**), JX14T (**D**), and JX39P(**E**) were modeled with GeneGo MetaCore™ direct-interaction or auto-expand < 20 node networks. Uploaded kinases are indicated with circles as RTS increased (red) or decreased (blue). Lines between nodes indicate interactions with color indicating type (green; positive, red; negative; grey; other). PDX tumor cells were grown as neurospheres and viability was measured after 7-day treatment (500nM sitravatinib or brigatinib) with CellTiter-Glo® in (**F**) and displayed as percentage of vehicle control with bars for SEM, with *** indicating p<0.0001 calculated using two-way ANOVA.

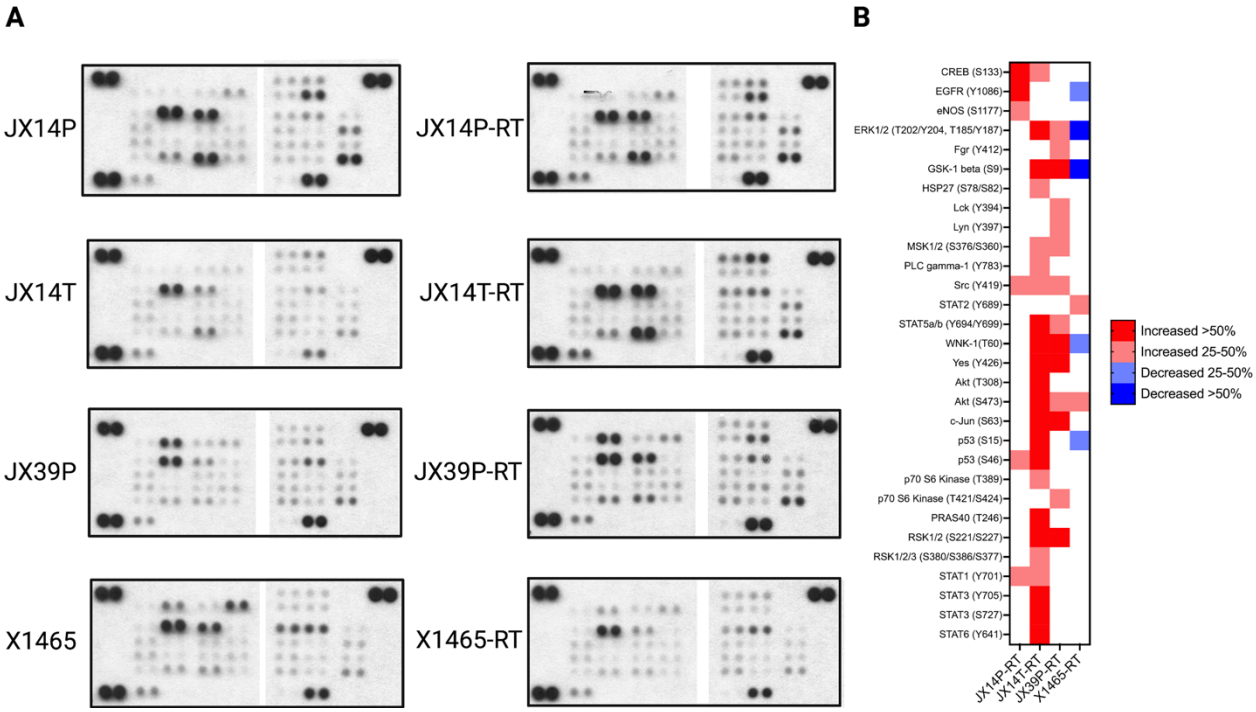

Figure 6. Phosphokinase Western blot array shows differential phosphorylated proteins in GBM PDX-RTS pairs. (**A**) R&D Systems Proteome Profiler Human Phospho-Kinase Arrays for RTU and RTS pairs for JX14P, JX14T, JX39P and X1465 shown with equal protein loading. (**B**) Heatmap showing relative change in phospho-antibody spot intensity with at least 25% difference as compared to parent tumor signal.